AIAA SciTech Forum
6-10 January 2020, Orlando, FL
AIAA Scitech 2020 Forum

10.2514/6.2020-0683

Filtering of Acoustic Disturbances from Aero-Optical Measurements

Brian L. Catron*, R. Mark Rennie†, Stanislav Gordeyev‡, Eric J. Jumper§
University of Notre Dame, Notre Dame, IN, 46656

The performance of an airborne optical system can be degraded by optically-active flows such as compressible boundary layers, shear layers and shock waves. Recent research shows that optical performance can also be affected by the local acoustic field, which also needs to be taken into account in order to determine the deployed performance of a given system. One of the primary contamination sources of optical wavefronts in wind-tunnel measurements is the duct acoustic field that forms in the wind-tunnel test section in response to the main fan. This paper presents an investigation into the impact of tunnel acoustics on wavefront measurements. The important acoustic modes are determined using theory, and it is shown that the amplitudes of the important acoustic modes can be determined by examining the spatial frequency content of a wavefront data at a given temporal frequency.

Nomenclature

Ap	=	Aperture diameter
c_0	=	Speed of sound based on average fluid properties
f	=	Temporal frequency
I	=	Intensity of light
I_0	=	Intensity of light in the diffraction-limited case
k	=	Wavenumber
k_0	=	Total acoustic wavenumber ($k_0 = \omega/c_0$)
K_{GD}	=	Gladstone-Dale constant, 2.27×10^{-4} m^3/kg
M	=	Mach number
n	=	Index-of-refraction
OPD	=	Optical path difference
OPD_{rms}	=	Spatial rms value of an optical path difference
$p_m^{\pm}$	=	Acoustic mode coefficient
p_0	=	Reference pressure for sound pressure level measurements
SR	=	Strehl ratio
γ	=	Angle of the beam in the test section
λ	=	Wavelength of light
Λ	=	Acoustic wavelength
ξ	=	Spatial frequency
$\Psi_m(x, y)$	=	Characteristic function of a duct
ω	=	Angular frequency
$'$	=	Fluctuating quantity of a property
$_B$	=	Beam coordinate frame
$_D$	=	Duct coordinate frame
$\hat{}$	=	Complex quantity of a property

*PhD Candidate, Department of Aerospace and Mechanical Engineering, Hessert Laboratory for Aerospace Research, Notre Dame, IN 46656, AIAA Student Member.
†Research Associate Professor, Department of Aerospace and Mechanical Engineering, Hessert Laboratory for Aerospace Research, Notre Dame, IN 46656, AIAA Senior Member.
‡Associate Professor, Department of Aerospace and Mechanical Engineering, Hessert Laboratory for Aerospace Research, Notre Dame, IN 46656, AIAA Associate Fellow.
§Professor, Department of Aerospace and Mechanical Engineering, Hessert Laboratory for Aerospace Research, Notre Dame, IN 46656, AIAA Fellow.

I. Introduction

A. Aero-Optics

Optical communication and directed energy systems require a tightly focused beam on target in order to meet system performance objectives. The farfield performance of airborne optical systems can be degraded by the nearfield flow that becomes optically active at compressible flow speeds. "Aero-optics" is the study of the optical effect of these nearfield flow disturbances. Examples of important aero-optical flows that have been studied extensively include boundary layers [1–3], shear layers [4, 5], shock waves [6], and even tip vortices [7]. The effect of acoustic disturbances on aero-optical measurements has also been shown in both flight testing [8] and ground testing [9]. The Gladstone-Dale relationship shows how index-of-refraction, n, of a fluid changes with its density, ρ:

$$n'(\vec{x},t) = K_{GD}\rho'(\vec{x},t), \tag{1}$$

where K_{GD} is the Gladstone-Dale constant which has a value of approximately 2.27×10^{-4} $\mathrm{m^3/kg}$ for light at visible and near-IR wavelengths and $'$ represents the use of fluctuating quantities. The optical aberrations are typically evaluated by their effect on an interrogating beam of light with a known initial wavefront that passes through the region of interest. An instrument such as a Shack-Hartman wavefront sensor is used to measure the spatially-resolved integration of the index-of-refraction over a distance traversed by the light beam:

$$\mathrm{OPD}(x,y,t) = \int_{s_1}^{s_2} n'(\vec{x},t)ds, \tag{2}$$

where OPD is the optical path difference which is the conjugate of the wavefront.

The farfield performance of an airborne optical system can be estimated via the Maréchal approximation:

$$\mathrm{SR}(t) \equiv \frac{I(t)}{I_0} \approx \exp\left\{-\left[\frac{2\pi\mathrm{OPD}_{rms}(t)}{\lambda}\right]^2\right\}, \tag{3}$$

where SR is the Strehl ratio, $I(t)$ is the intensity on target, $\mathrm{OPD}_{rms}(t)$ is the spatial root mean square of the OPD at time t, and λ is the wavelength of the light. The diffraction-limited on target intensity, I_0, for a beam with a circular cross section is given via:

$$I_0 = \left(\frac{kAp^2}{8z}\right)^2, \tag{4}$$

where k is the wavenumber ($k = 2\pi/\lambda$), Ap is the aperture diameter, and z is the distance to the aperture. The Strehl ratio represents how well an optical system performs versus the diffraction-limited case. Equations 3 and 4 are shown as a function of wavelength in Figure 1. The left subplot shows how the Strehl ratio decreases significantly as the wavelength decreases with a constant optical disturbance. The right subplot shows that as the wavelength is decreased the diffraction-limited performance exponentially increases. These two plots illustrate the aero-optics problem as a whole, and why there is a desire to transition airborne optical systems to shorter wavelengths to take advantage of the diffraction-limited performance gain; however, to achieve this the optical disturbance must also be greatly reduced.

B. Duct Acoustics

Acoustic waves are isentropic compression waves that propagate at the speed of sound, c_0, in the local medium [11]. If the acoustic waves are in a fluid with some mean flow, the acoustic waves travel relative to the mean flow such that the observed speed is $u \pm c_0$. The fluctuating pressure, p', associated with acoustic signal can be measured with a microphone. A common way of reporting the strength of an acoustic waves is the sound pressure level,

$$\mathrm{SPL} = 20\log_{10}\frac{p_{rms}}{p_0}\ \mathrm{dB}, \tag{5}$$

where p_{rms} is the root-mean-square of the fluctuating pressure and p_0 is the reference pressure which is typically defined as the threshold of human hearing and for air is 20 μPa [12]. The density fluctuation in an acoustic wave can be related to a pressure fluctuation via the definition of the speed of sound,

$$c_0^2 = \left(\frac{\partial p}{\partial \rho}\right)_s = \frac{p'}{\rho'}. \tag{6}$$

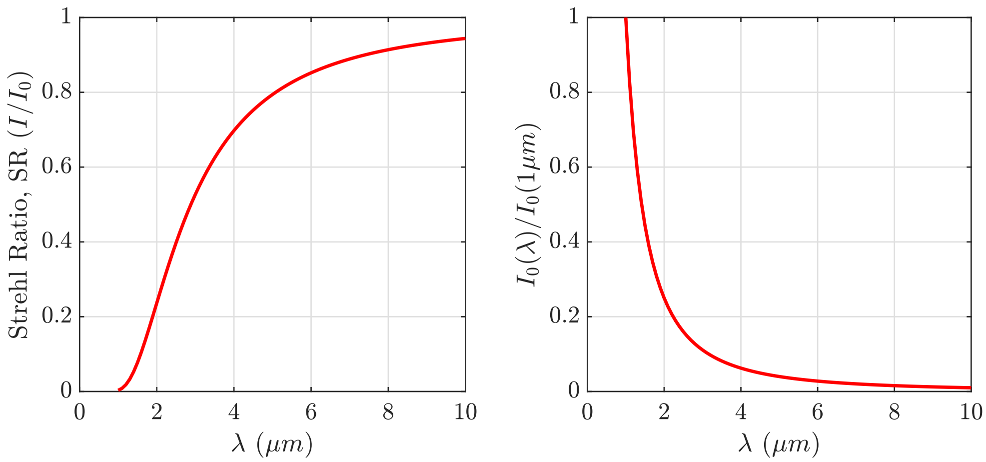

Figure 1 Summary of the aero-optics problem. The left plot shows a 95% Strehl Ratio (Equation 3) at 10.6 μm corresponding to estimates from the ABL program [10]. The right plot show the diffraction-limited on target intensity (Equation 4) relative to the performance of a 1 μm wavelength beam.

By assuming an inviscid flow with constant mean quantities in both space and time the convecting wave equation can be derived from the conservation of mass and momentum equations. The convecting wave equation [13],

$$\left(\frac{1}{\omega^2}\frac{\partial^2}{\partial t^2} - \frac{1-M^2}{k_0^2}\nabla^2\right)p = 0, \tag{7}$$

is used to describe duct acoustics with flow in the axial direction of a constant-area duct when the length is much greater than the cross-sectional dimensions. Using the assumption that the pressure field is separable (i.e. $p(x,y,z,t) = p(x,y)p(z)p(t)$), the solution in complex notation is [14]

$$\hat{p}_m(\mathbf{x},t) = \sum_{m=0}^{\infty} \Psi_m(x,y)\left(p_m^+ \exp\left\{-jk_{zm}^+ z\right\} + p_m^- \exp\left\{+jk_{zm}^- z\right\}\right)\exp\left\{j\omega t\right\}, \tag{8}$$

where $p_m^\pm$ are the upstream and downstream modal coefficients, $k_{zm}^\pm$ are the axial-wavenumbers in each direction. The characteristic function of the duct for the mth mode, $\Psi_m(x,y)$, is an eigen-function solution to the two-dimensional Helmholtz equation,

$$\left(\frac{\partial^2}{\partial x^2} + \frac{\partial^2}{\partial y^2}\right)p_{xy}(x,y) + k^2 p_{xy}(x,y) = 0. \tag{9}$$

Solving the Helmholtz equation requires boundary conditions to be placed on the duct walls. A common boundary condition is for rigid walls that perfectly reflect incident waves,

$$\nabla p_{xy}(x,y)\cdot\mathbf{n}_{wall} = 0. \tag{10}$$

There are infinitely many characteristic functions that satisfy Equations 9 and 10 each of which has a characteristic wavenumber, k_m, which is the eigen-value of the Helmholtz solution. The wavenumber in the axial direction for a duct with mean flow is

$$(k_0 \pm M k_{zm}) = k_m^2 + k_{zm}^2, \tag{11}$$

where k_0 is the total wavenumber ($k_0 = \omega/c_0$) and k_{zm} is the axial wavenumber. The axial wavenumber will have two solutions for cases when there is mean flow,

$$k_{zm}^\pm = \frac{\mp M k_0 + \sqrt{k_0^2 - (1-M^2)k_m^2}}{1-M^2}. \tag{12}$$

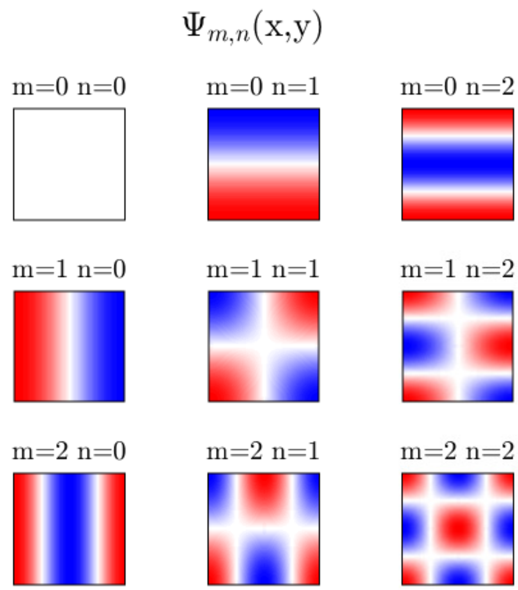

Figure 2 Characteristic functions for a rectangular duct for the modes $m = 0 \ldots 2$ and $n = 0 \ldots 2$.

For the acoustic wave to propagate indefinitely, the quantity under the square root must be greater than or equal to zero. This results in certain modes only existing above a certain frequency known as the cut-on frequency,

$$f_{cuton} = \frac{c_0}{2\pi}\sqrt{(1 - M^2)k_m^2}. \tag{13}$$

Below this frequency an acoustic mode will be exponentially attenuated as it travels through the duct.

This study will examine a simple rectangular geometry which has a known set of characteristic functions given by

$$\Psi_{m,n}(x, y) = \cos\left(\frac{m\pi x}{l_x}\right)\cos\left(\frac{n\pi y}{l_y}\right), \tag{14}$$

where l_x is the duct width or depth and l_y is the duct height. For this geometry the modal wavenumber, k_m, is a combination of the wavenumber in both the x and y directions,

$$k_m^2 = k_x^2 + k_y^2. \tag{15}$$

Some of the characteristic functions for a rectangular duct are shown in Figure 2.

II. Experimental Results

Wavefront measurements were conducted in the University of Notre Dame White Field Wind Tunnel facility at Mach Numbers of 0.5 and 0.6 and were previously discussed by Catron [9]. The wind-tunnel test section had high-speed inserts installed giving cross-sectional dimensions of 31-inches high and 36-inches wide. The wavefronts were recorded using a double pass setup where a 10-inch diameter beam passed through the test section and was reflected back along the same path. The beam was re-imaged to a size of 5/8-inch diameter onto the lenslet array of a Shack-Hartman wavefront sensor with a lenslet pitch of 30-μm on a square grid. This resulted in the wavefront being measured over an approximately 55-lenslet diameter at a sample rate of 34000-Hz. A Nd-YAG laser at 532-nm was the light source.

The aperture-averaged power spectra of the measured wavefront aberrations are presented in Figure 3. The spectra for both Mach number cases contain between six and eight obvious peaks that can be associated with acoustic waves originating from the tunnel fan. The peaks at 459 Hz for M=0.5 and 536 Hz for M=0.6 correspond to the blade-passing frequency from the tunnel fan with the other peaks representing harmonics of the blade-passing frequency. The

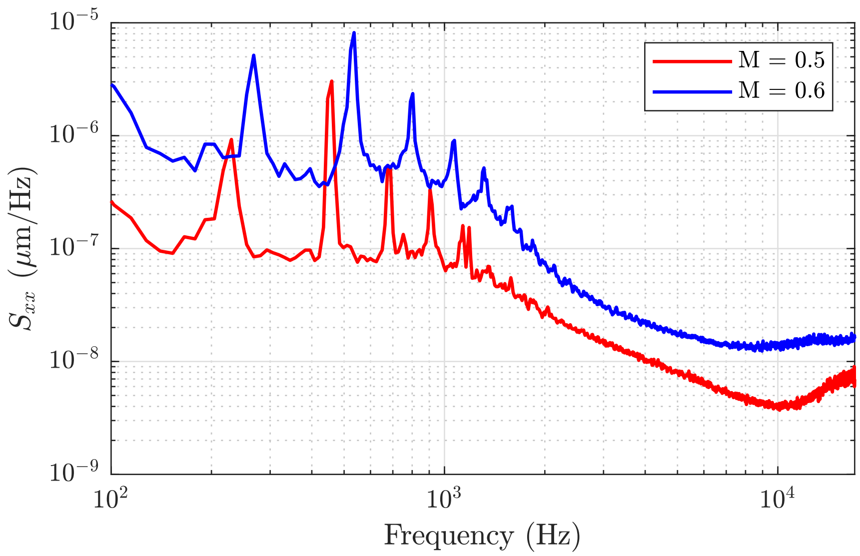

Figure 3 Power Spectra of the measured wavefront at Mach Numbers 0.5 and 0.6.

blade-passing frequency peaks are by far the most predominant with the sub-harmonic being the second most. The M=0.6 case shows more broadband noise than the M=0.5 case.

For the rest of the paper only the M=0.6 case will be examined. The dispersion spectra can be seen in Figure 4 which consist of the temporal spectra and two spatial spectra (i.e. horizontal and vertical) of the wavefront data as computed by,

$$S_{xx} = \frac{|\text{FFTn(OPD)}|^2}{N \cdot \prod f_{samp}}, \tag{16}$$

where FFTn is the N-Dimensional Fourier Transform, N is the total number of sample points, and $\prod f_{samp}$ is the product of the spatial and temporal sample rates. For the analysis in this paper, the OPD array was placed into a larger array of zeros 2 times larger in the spatial directions and 1.5 times larger in the temporal direction prior to calculating the fft. The plot on the left shows the component of the optical disturbances that is moving horizontally through the measurement beam with the top half moving in the direction of the flow and the bottom half moving upstream. The horizontal dispersion plot has three main features with the first being the significant broadband signal that is convecting with the flow and is associated with the boundary layer. The second feature is a significant broadband signal that is moving upstream at $u - c_0$, that will be discussed in detail below. The third feature is the strong vertical "spikes" at the blade-passing frequency and its harmonics with six strong peaks exhibiting broadband spatial frequencies over the entire spatial frequency space. Several additional blade-passing frequency harmonics can be observed along the horizontal spatial frequency axis. The white lines overlaid on the plot represent the acoustic lines associated with various modes where $m = 0$. There is noticeable increase in the wavefront signal when each mode cuts-on.

The plot on the right shows the component of the optical disturbances that are moving vertically through the beam with the top half moving up and the bottom half moving down with the overlaid white lines representing the acoustic lines. The vertical spectral plot is symmetric about the zero vertical spatial frequency line. The extra spatial content when a mode cuts-on is noticeable outside of the acoustic lines in both directions. Both horizontal and vertical dispersion plots show significant spikes at the blade-passing frequency and its various harmonics.

III. Analysis

An analysis of acoustic modes can be made by looking at a single slice of the dispersion array. A slice of the dispersion array taken at the blade-passing frequency is shown in Figure 5. Most of the spectral content of the slice is moving upstream (on the negative horizontal spatial frequency side) and is fairly symmetric about the zero vertical spatial frequency line. To compare with the experimental data in Figure 5, artificial optical wavefronts were generated by 'shooting' a beam through the density field of the acoustic modes given by Equations 8 and 14. The geometry for the creation of the artificial wavefronts is shown in Figure 6. The duct coordinate frame is centered on the beam entrance to

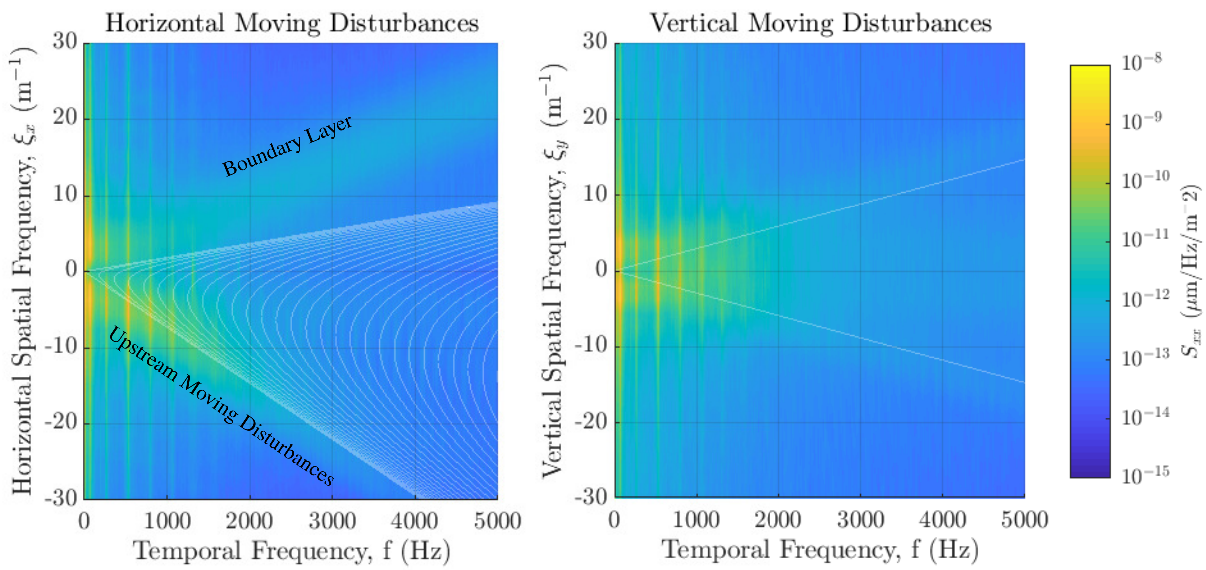

Figure 4 Dispersion analysis of the wavefronts measured at M=0.6. The left plot shows the spectral content moving horizontally with modal acoustic lines corresponding to $m = 0$ and $n = 0...30$. The right plot shows the spectral content moving vertically with the acoustic lines shown.

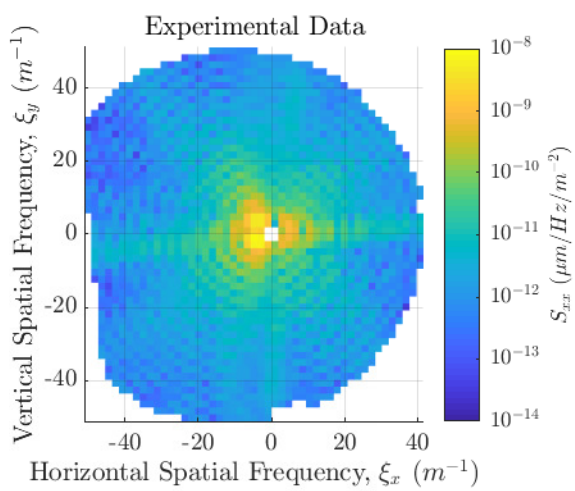

Figure 5 Slice of the dispersion array taken at the blade-passing frequency.

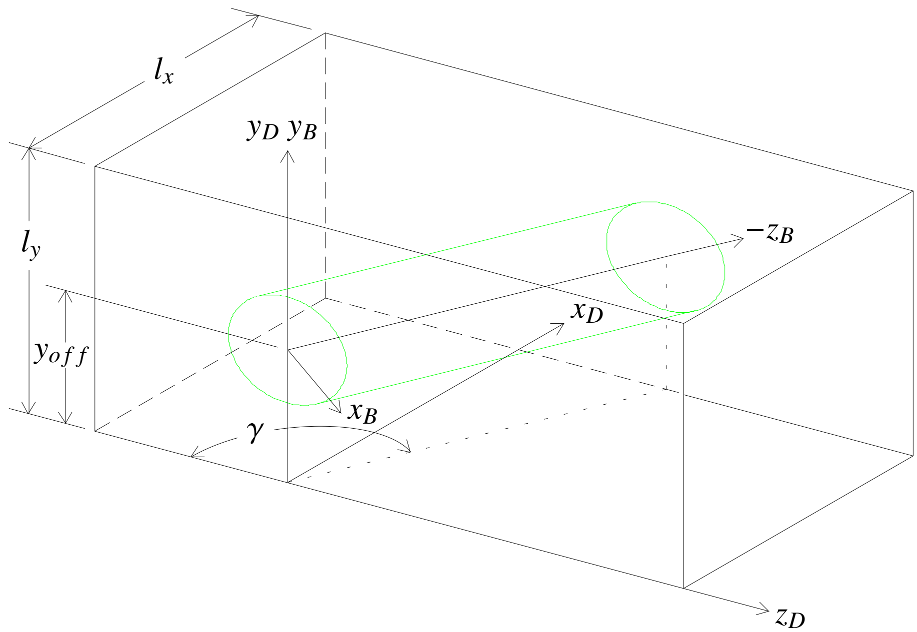

Figure 6 General geometry for calculation presented in this paper.

the duct in the z-direction and positioned on the wall of the duct such the duct lays in positive x and y space. The duct has a height of l_y and a depth of l_x. The beam coordinate frame is centered on the beam with the y-axis co-axial to the y-axis of the duct and the beam propagating along the -z-axis. The angle that the beam goes through the duct is denoted by γ and represents the rotation of the beam coordinate frame compared to the duct coordinate frame. The xz-planes of the two coordinate frames are separated by y_{off}, which in this study is half the height of the duct. Transitioning from the beam coordinate frame to the duct coordinate frame is a simple rotation about the y-axis after the offset is added to the beam coordinates.

$$\begin{bmatrix} x_D & y_D & z_D \end{bmatrix} = \begin{bmatrix} x_B & y_B + y_{off} & z_B \end{bmatrix} \begin{bmatrix} \cos\gamma & 0 & -\sin\gamma \\ 0 & 1 & 0 \\ \sin\gamma & 0 & \cos\gamma \end{bmatrix} \tag{17}$$

The artificial wavefronts were generated by first calculating the complex pressure field with zero phase and time at and around the blade-passing frequency using Equations 8, 12, and 14. The complex optical path difference for each pressure field can be determined by integrating across the duct,

$$\widehat{\mathrm{OPD}}(x_B, y_B) = \frac{K_{GD}}{c_0^2} \int_0^{l_x} \hat{p}(x_D, y_D, z_D) dx_D. \tag{18}$$

This complex OPD only contains magnitude and phase information and not temporal information which can be obtained from the real component of the complex OPD multiplied by $\exp\{j\omega t\}$,

$$\mathrm{OPD}(x_B, y_B, t) = \Re\left(\widehat{\mathrm{OPD}}(x_B, y_B)\exp\{j\omega t\}\right). \tag{19}$$

The acoustic modes that are present in the test section at a given frequency can be determined by inserting the frequency into Equation 13, and is shown graphically for the blade-passing frequency in Figure 7. At the blade-passing frequency this figure shows that there are only 12 possible acoustic modes that can propagate indefinitely in the test section. Additionally, for a beam angle of $\gamma = 90°$, the acoustic modes that have an integer number of half wavelengths across the test section will produce no optical aberrations, since $\int_0^1 \cos(m\pi x)dx = 0$ when $m \neq 0$, so that only 4 acoustic modes actually need to be examined at this frequency. In general this would not be the case at other viewing angles except in the case where a mode has perfect combination of equal positive and negative pressure fluctuations across the beam path.

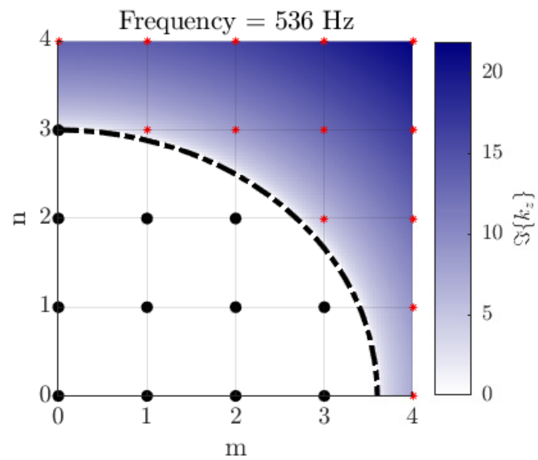

Figure 7 Possible acoustic duct modes for the blade-passing frequency.

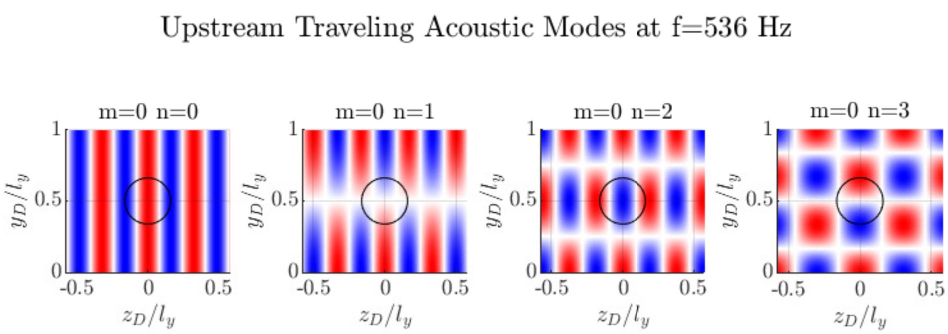

Figure 8 Optical aberrations from the four upstream traveling acoustic modes that were examined.

The optical aberrations from the four upstream traveling acoustic modes that were examined are shown in Figure 8. The figure also shows the outline of the measurement beam in relation to the overall duct. As the mode number increases the axial wavelength also increases for the upstream traveling waves. The opposite is true for the acoustic waves traveling in the direction of the flow. At the cut-on frequency, the axial wavelengths would be equal for the upstream and downstream traveling acoustic waves.

A set of spectral slices were next computed at the blade-passing frequency for each unit normal acoustic mode wavefront for fitting to the experimentally measured spectral slice shown in Figure 5. The results for two different cases are shown in Figure 9. The two different cases involve acoustic modes produced at one frequency bin or at three different frequency bins with one being on either side of the frequency being studied. The single frequency bin fit and the three frequency bin fit appear to be visually identical and very similar to the experimentally measured one in Figure 5. The experimental spectral slice is a bit smoother but this is likely due to the simulated wavefronts being computed along a single ray at the center of each lenslet instead of being integrated over the entirety of the lenslet. The generated spectral slices are perfectly symmetric about the $\xi = 0m^{-1}$ line, while the experimental slice is slightly asymmetric which could be the result of the beam being slightly off center vertically in the tunnel. The only structure missing from the generated spectral slices is a plus shaped signal laying along both axes. These could be the result of standing waves that may have formed in the test section.

The spectral slices scale by the square of the modal coefficient. The resultant coefficient magnitudes for the acoustic

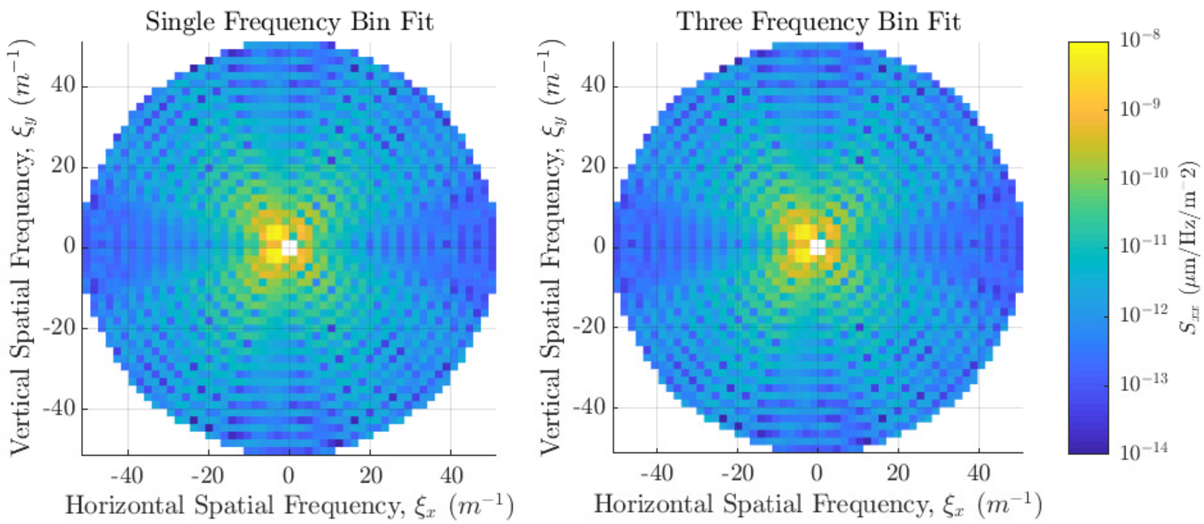

Figure 9 Best fit dispersion slices for (left) only the blade-passing frequency and (right) the blade-passing frequency and the frequency bin on either side.

Mode	1 Bin	3 Bins
$p^-_{0,0}$	1.56	0.87
$p^-_{0,1}$	25.86	23.85
$p^-_{0,2}$	1.67	0.42
$p^-_{0,3}$	1.55	1.51
$p^+_{0,0}$	0.58	1.40
$p^+_{0,1}$	1.14	1.91
$p^+_{0,2}$	1.38	0.42
$p^+_{0,3}$	0.37	1.38

Table 1 Acoustic mode coefficient magnitudes at the blade-passing frequency

modes present at the blade-passing frequency are shown in Table 1. For both cases, the upstream traveling $p^-_{0,1}$ acoustic mode was the most prevalent. There was no pattern when going from one frequency bin to three other than 5 of the 8 modes decreased in magnitude, but these changes were inconsistent in relative magnitude. Trying to account for the frequency bins having some signal overlap is likely only necessary when computing the actual pressure field instead of removing the acoustic information from the measured spectral slice. Some of the larger differences in the coefficient magnitudes maybe due to different starting guesses converging to separate local minima regions. Using spectral slices to determine modal coefficients only results in the magnitude being known. Phase cannot be computed this way.

IV. Conclusion

This paper has set out a process by which the strength of acoustic duct modes in a wind-tunnel test section can be estimated from measured wavefronts in the spectral domain. These estimates can be used to statistically correct the measured duct modes for the optical effect of the tunnel acoustic modes. For the purpose of removing the duct acoustics from a single spectral slice, only the spectral information of the acoustic modes present at that frequency would be necessary to compute. In order to recreate a pressure field multiple frequency bins worth of spectral information would likely need to be considered if the frequency bins are close enough that there could be some overlap in the spectral domain by the various modes. The recreation of the exact pressure signal would require phase information to be known which is beyond the scope of this paper, but the root-mean-square values could be easily determined. The acoustic equations presented in this paper assume a constant cross-section but by relaxing some of the assumptions needed to derive the convecting wave equation this method should be extendable to three-dimensional mean flow fields if the suitable 'duct' characteristic functions can be determined.

References

[1] Gordeyev, S., Smith, A. E., Cress, J. A., and Jumper, E. J., "Experimental Studies of Aero-Optical Properties of Subsonic Turbulent Boundary Layers," *Journal of Fluid Mechanics*, 2014. doi:10.1017/jfm.2013.658.

[2] Smith, A. E., Gordeyev, S., and Jumper, E. J., "Recent Measurements of Aero-Optical Effects Caused by Subsonic Boundary Layers," *Optical Engineering*, 2013. doi:10.1117/1.OE.52.7.071404.

[3] Wang, K., and Wang, M., "Aero-Optics of Subsonic Turbulent Boundary Layers," *Journal of Fluid Mechanics*, 2012. doi:10.1017/jfm.2012.11.

[4] Fitzgerald, E. J., and Jumper, E. J., "The Optical Distortion Mechanism in a Nearly Incompressible Free Shear Layer," *Journal of Fluid Mechanics*, 2004. doi:10.1017/S0022112004009553.

[5] Rennie, R. M., Duffin, D. A., and Jumper, E. J., "Characterization and Aero-Optic Correction of a Forced Two-Dimensional Weakly Compressible Shear Layer," *AIAA Journal*, 2008. doi:10.2514/1.35290.

[6] Jumper, E. J., Zenk, M. A., Gordeyev, S., Cavalieri, D., and Whiteley, M. R., "Airborne Aero-Optics Laboratory," *Optical Engineering*, 2013. doi:10.1117/1.OE.52.7.071408.

[7] Porter, C., Rennie, M., and Jumper, E., "Aero-Optic Effects of a Wingtip Vortex," *AIAA Journal*, 2013. doi:10.2514/1.J050899.

[8] De Lucca, N., Gordeyev, S., Jumper, E. J., and Wittich, D. J., "Effects of Engine Acoustic Waves on Optical Environment Around Turrets In-Flight on AAOL-T," *Optical Engineering*, 2018. doi:10.1117/1.OE.57.6.064107.

[9] Catron, B. L., Rennie, M. R., Gordeyev, S., and Jumper, E. J., "Effect of Acoustic Disturbances on Aero-Optical Measurements," *2018 Plasmadynamics and Lasers Conference*, 2018. doi:10.2514/6.2018-3903.

[10] Jumper, E. J., and Gordeyev, S., "Physics and Measurement of Aero-Optical Effects: Past and Present," *Annual Review of Fluid Mechanics*, 2017.

[11] Bose, T., *Aerodynamic Noise - An Introduction for Physicists and Engineers*, Springer, 2013.

[12] Randall, R. H., *An Introduction to Acoustics*, Addison-Wesley Press Inc., 1951.

[13] Munjal, M. L., *Acoustics of Ducts and Mufflers*, 2$^{\text{nd}}$ ed., John Wiley & Sons Ltd, 2014.

[14] Jacobsen, F., and Juhl, P. M., *Fundamentals of General Linear Acoustics*, John Wiley & Sons Ltd, 2013.